Pentafrequency Resonator based on a CRLH Microstrip for Multinuclear MRI and MRS at 7 T

Daniel Hernandez*

Gachon University, Incheon 21936, Republic of Korea

In this study, we present a transmission-line design based on the concept of composed right- and left-hand microstrip (CRLHTL) that is able to produce a uniform B_1 field at five different frequencies. The design uses the same conductor line for all five frequencies, and maintains a uniform field along the Z axis. The CRLH concept is used to ensure that the line is operating with a uniform propagation constant in a lossless scenario. We performed electromagnetic simulations to validate the design.

Keywords : pentafrequency resonator, magnetic resonance imaging/magnetic resonance spectroscopy, multinuclear, microstrip antenna

1. Introduction

The use of magnetic resonance imaging (MRI) has tremendous diagnostic importance pertaining to the treatment of the human body. In comparison with other imaging techniques, MRI allows the study of the human metabolism and functions [1-5]. High-quality anatomical and functional images can be acquired with MR systems at increased field strengths, such as 7 T. These images are mostly acquired based on the resonance of protons in water molecules inside the body [6]. The frequency at which these protons resonate is known as the Larmor frequency and constitutes a physical property of the nuclei [7]. In addition to proton ^{1}H, there are other nuclei that can resonate to produce signals and images in MRI, such as fluorine (^{19}F), potassium (^{31}P), lithium ([7]Li), and sodium ([23]Na) [8-10]. These nuclei (also known as X-nuclei) have resonant frequencies at 280 MHz (^{19}F), 121 MHz (^{31}P), 116 MHz ([7]Li) and 78 MHz ([23]Na) in a 7T MRI system.

[19]F is one of the nuclei that can be used as an MR tracer given that it has a Larmor frequency similar to ^{1}H, a natural abundance of 100 %, and a sensitivity of 83 % compared with the hydrogen nucleus. Early studies in 1977 [11] documented the use of ^{19}F MR for the imaging.

Despite the fact that in the study the sensitivity was low because of the low-field, imaging feasibility was proven possible. Advances in MRI technology have been documented with MR systems with strong magnets (such as 7 T) wherein higher sensitivities can be achieved. For instance, *in vivo* cell tracking using ^{19}F MRI [12], cell labeling [13], and *in vivo* quantification [14, 15] have been proposed and implemented with ^{19}F MRI. [19]F MRI can also be used as a tool for drug investigations and their reactions associated with the metabolism in the body, such as for instance, anticancer drugs monitored with MRI [16]. Another application is functional lung MRI with fluorinated gases [17]. The use of ^{19}F as a contrast agent for imaging and MRS has many applications. Accordingly, with the use of stronger magnets the challenge of low-signal sensitivity can be overcome [18].

[7]Li is another nucleus that can be detected and imaged with MRI, however, its low sensitivity compared with proton makes its imaging challenging [19]. Nevertheless, there is a considerable interest to study the concentrations of lithium in the brain, as they are related with disorders that affect the way a person feels or thinks, such as bipolar disorders [20].

[31]P is mostly linked to metabolic processes inside the body. Its has been proposed that the use of MRI and MRS can study tissue metabolism in a noninvasive form [21, 22]. The limitations of ^{31}P are also related to its low sensitivity compared with proton, and its complex spectral pattern. To obtain images with good signal-to-noise (SNR),

*Corresponding author: Tel: +82-32-820-4246
Fax: +82-32-820-4246, e-mail: danmri@gachon.ac.kr

it is necessary to scan for a long time that is prohibitive for clinical use given the patient's inability to maintain a still posture for prolonged time periods.

[23]Na has the lowest Larmor frequency from all the other nuclei described above. However, it is possible to obtain brain [23]Na images with resolutions of the order of $1\times1\times5$ mm^3 or $4\times4\times4$ mm^3 at acquisition times of approximately 10 to 35 minutes [23]. The interest in brain sodium studies relates to the analysis of neurodegenerative diseases, such as multiple sclerosis [24] and Alzheimer's disease [25].

1.1. Multinuclear Coils

Given the need to study each of the aforementioned nuclei, it is important to develop the hardware capable of acquiring signals and reconstructing images. The RF coils that can work at different frequencies have already been proposed [26-30]. It is commonly needed to conduct proton imaging for correlation with the nuclei signals and images. For this reason, it is desired that the same coil is used to operate at multiple frequencies. Various types of coils have been proposed that have used loop array coils, microstrips, and combination of different types of resonators [31-36].

The use of array elements is desired because they can produce a uniform B$_1$ field when they operate in a circularly polarized mode in which the phase of each of the resonant elements is added constructively to increase the field uniformity. However, in multifrequency coils, the number of elements is increased [37]. Typically, an array φ_f that can produce a uniform B$_1$ field consists of n resonating elements (either a loop coil or microstrip lines), but when a multifrequency coil is designed, the total number of elements N$_e$ will increase by,

$$N_e = \Sigma_{f=1}^{n} \varphi_f \tag{1}$$

In the case that the number of elements per array at each frequency is the same, then the total number would be

$$N_e = \varphi \times n \tag{2}$$

The increased number of elements can become a challenge [38-40] when the coupling between the elements is considered. The coupling between coils could become a problem for the SNR response and for parallel imaging [41], whereby the algorithms need to use unique field maps to reconstruct the undersampled data.

Several studies have shown methods for decoupling elements in array coils, either by using LC circuits [42], active circuits [43], using passive components [44], or geometrical decoupling [45]. Even though numerous elements have been used to achieve decoupling in a

multiple element array [46], the circuitry and complexity increases.

According to Roemer *et al.* 1990, the theoretical optimal overlap distance between two circular loop coils is 0.25 times the diameter of the coil and conductor width of 0.01 the size of the coil [47]. These optimal values would be difficult to obtain in the case of multilayer arrays for multifrequency operations due to the multiple elements that need to be optimized for each frequency to provide strong and uniform B$_1$ field.

The field intensity and uniformity are also affected by the distance of the RF element to the imaging object. Placing the coils farther away from the anatomical region of interest will yield lower signal intensities. Given that the signal sensitivity of the X-nuclei is already small, the position of the coil should be considered to optimize the signal.

We propose a solution to this challenge by using a microstrip coil combined with a basic idea from composite right-left handed transmission lines that is able to produce uniform and high intensity |B$_1$| fields at each of the frequencies of interest. In this way, the same microstrip can be used for imaging and acquisition of signals from multiple frequencies and nuclei by simply changing the matching circuit.

2. Methods

The use of microstrips in MRI has also been proposed given their various advantages [48] and abilities to produce a uniform B$_1$ field along the Z-Y plane. It has been shown that decoupling microstrips are also better than loop coils [49]. The circuit diagram representing a lossless microstrip is shown in Fig. 1(a). The microstrip consist of a series inductance L$_R'$ and a parallel capacitor C$_R'$, where the accent (') indicate its dependence on length. The subscript (R) indicates the right-handed or natural occurring properties of the transmission line. The performance of a microstrip is highly dependent on its geometry. According to the general equations for microstrips,

Propagation constant: $\sqrt{\gamma = (R + j\omega L)(G + j\omega C)}$ (3)

Attenuation constant: $\alpha = R\{\gamma\}$ (4)

Phase constant: $\beta = F\{\gamma\}$ (5)

Wavelength: $\lambda = \dfrac{2\pi}{|\gamma|}$ (6)

The dependence on the capacitance and inductance is based on the length and width of the conductor's line and
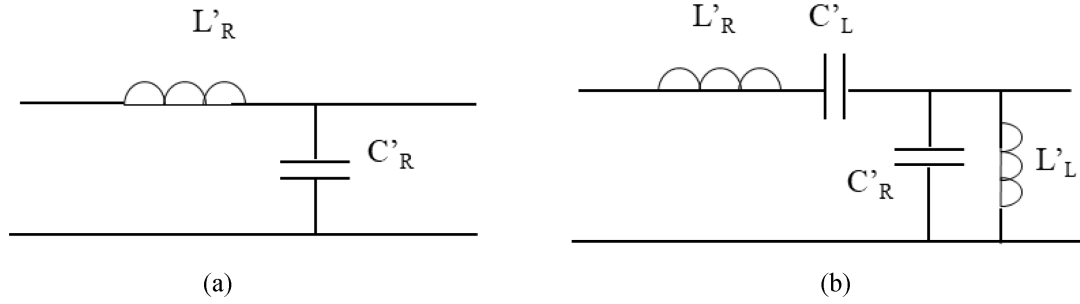
Fig. 1. Circuit representation of the (a) microstrip line and (b) the composed right- and left-hand microstrip (CRLH TL).

height between the ground plane and the conductor line, as well as the dielectric material's relative permittivity.

The main reason that the field uniformity is dependent on the length and geometry is the wavelength and phase of the signal along the line. The current intensity will be reduced as the frequencies are shifted away from the center tuning frequency.

To solve this problem, the uses of composite right-left hand (CRLH) transmission lines have been investigated [50-53]. CRLH have properties that modify the wavelength and phase constant of the transmission line. Figure 1(b) shows the basic diagram of a CRLHTL, which consists of a transmission line with right-handed properties given by series inductance L_R' and parallel capacitance C_R', and left-handed (L) properties that are artificially added to the transmission line, as a series capacitance C_L' and parallel inductance L_L'. Whereby the correspondent equations are,

$$\text{Propagation constant: } \gamma = \alpha + j\beta = \sqrt{Z'Y'} \qquad (7)$$

$$\text{Impedance: } Z'(\omega) = j\left(\omega L_R' - \frac{1}{\omega C_L'}\right) \qquad (8)$$

$$\text{Admittance: } Y'(\omega) = j\left(\omega C_R' - \frac{1}{\omega L_L'}\right) \qquad (9)$$

$$\beta(\omega) = s(\omega)\sqrt{\omega^2 L_R' C_R' + \frac{1}{\omega^2 L_L' C_L'} - \left(\frac{L_R'}{L_L'} + \frac{C_R'}{C_L'}\right)} \qquad (10)$$

$$s(\omega) = \begin{cases} -1 \text{ for } \omega < \omega\Gamma 1 = \min\left(\frac{1}{\sqrt{L_R'C_L'}}, \frac{1}{\sqrt{L_L'C_R'}}\right) \\ +1 \text{ for } \omega < \omega\Gamma 2 = \max\left(\frac{1}{\sqrt{L_R'C_L'}}, \frac{1}{\sqrt{L_L'C_R'}}\right) \end{cases} \qquad (11)$$

With the characteristic impedance given by,

$$Z_0 = \sqrt{\frac{L_L'}{C_L'}}\sqrt{\frac{L_R'C_L'\omega^2 - 1}{L_L'C_R'\omega^2 - 1}} \qquad (12)$$

Additionally, the wavelength is given by Eq. (6). As it can be observed, the wavelength can be controlled at different frequencies. Although the equations are given for a lossless case, they can provide an indication of the behavior of the transmission line.

The frequency boundaries are given by,

$$\frac{1}{\sqrt{L_R'C_L'}} \text{ and } \frac{1}{\sqrt{L_L'C_R'}} \qquad (13)$$

For example, consider the case of a microstrip and CRLHTL. Use of Eq. (7) allows the identification of some useful properties for the case of the lossless transmission line, the propagation constant, and impedance, for a transmission line with a series inductance of 26.6 nH, parallel capacitance of 108 pF, parallel inductance of 3 nH, and a series capacitance of 11 pF. Figure 2(a) shows the comparison of the phase constant for the microstrip and the CRLHTL. Figures 2(b) and (c) show the solution of the transmission Eq. (13) by substituting the propagation constant based on considerations of an open microstrip line (loading impedance equals infinity)

$$V(z) = V_0^+ e^{-\gamma z} + V_0^- e^{\gamma z} \qquad (14)$$

When excited at different frequencies, the curves exhibit a uniformity along the conductive line. Furthermore, the impedance (11) is shown in Fig. 2(d), wherein the two boundary frequencies for the frequency band that have uniform currents can be observed.

This equation shows that multiples frequencies can produce uniform current distributions in the case of the CRLHTL. However, in the case of the microstrip, the current follows a sinusoidal waveform.

We propose a transmission line based on the equations of the CRLHTL that will be able to produce uniform $|B_1|$ field at five different frequencies, wherein the frequencies are matched to the frequencies of the X-nuclei and proton at 80, 116, 121, 280 and 300 MHz, respectively for a 7 T MRI system. The concept is based on the generation of two frequency bands at which the transmission line
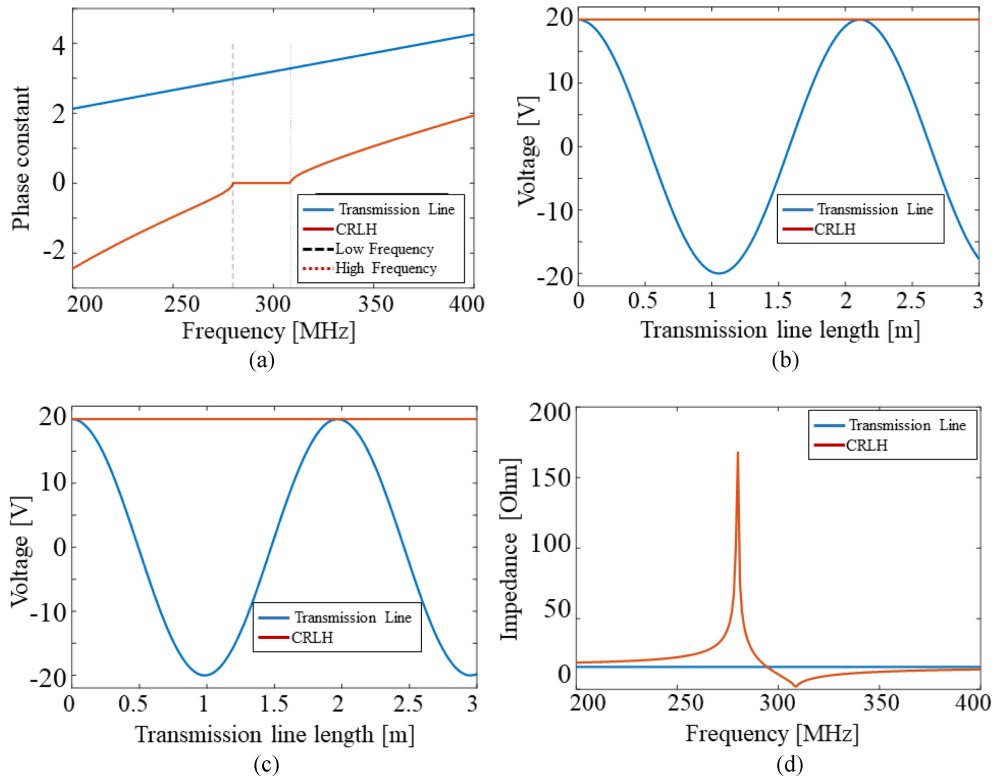
Fig. 2. (Color online) Comparison between the microstrip and CRLH for (a) phase propagation constant, (b) current waveform at 280 MHz, (c) current waveform at 300 MHz, and the (d) impedance of the transmission line.

produces a uniform field. One band would be designed to operate between 280 and 300 MHz, and the other between 80 to 121 MHz according to Eq. (10).

Use of CRLH has been proposed to distribute the lumped elements along the conductor line; however in the multifrequency applications it can sometimes generate
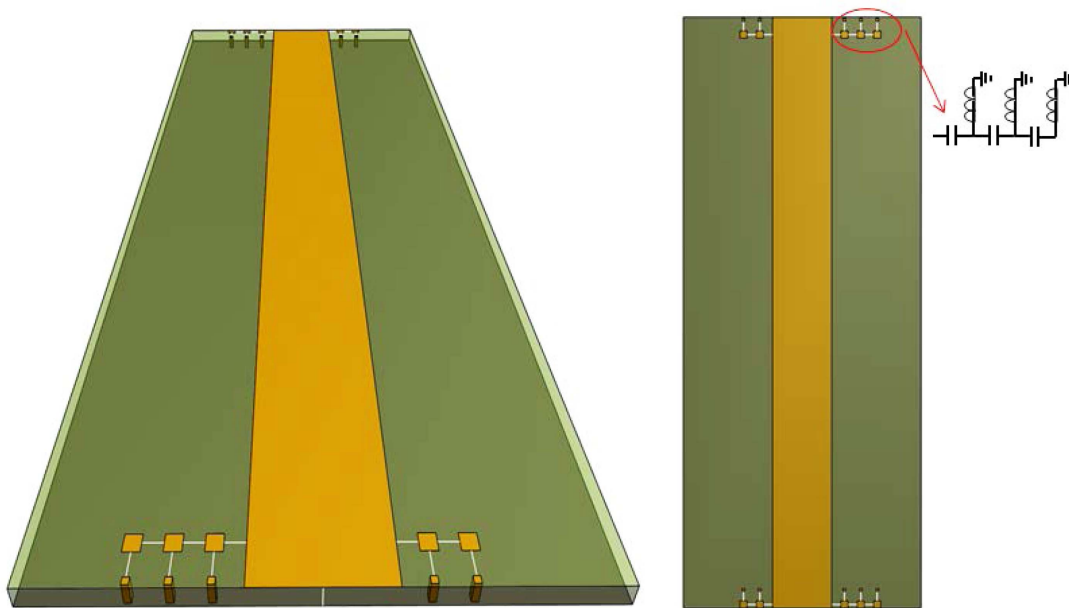

Fig. 3. (Color online) Three-dimensional (3D) model of the designed multifrequency transmission line with the use of lumped elements.

nonuniform field distributions. For this reason we opted to leave the strip line straight, and we added the lumped elements at the beginning and end of the strip line. The design of the microstrip line is shown in Fig. 3.

The transmission line consists of a dielectric material that separates the ground plane and the strip-line current, the dielectric material has a relative permittivity of 2.94 and a conductivity of 0.000668 S/m. The length of the transmission line is 200 mm, the width of the current line is 20 mm, the height of the dielectric material is 3 mm, and the lumped elements are added in two groups, namely, to the left and right of the strip line and at the start and end of the line. The circuit for the low frequencies consists of two series capacitors and two parallel inductors, and the circuits for the high frequencies have three series capacitors and three inductors. The capacitors are separated from the main line and from each other by 3 mm with a cooper plate with the dimensions of 2.5×2.5 mm, and the parallel inductors are connected from the center of the cooper plane to a vias connecting to ground.

The groups of circuits were tuned to two groups of frequencies. The first group consisted of the high frequencies 300 and 280 MHz, the lumped elements for these frequencies were located at the left of the transmission line, and both the circuit at the top and bottom parts of the line had identical values. In the same way, the circuits in the right were tuned to 80, 116, and 121 MHz.

In addition we acquired the $|B_1|$ field maps from the CRLH TL coil inside a human head model given by the human model DUKE from the virtual family provided by the EM simulation software [54]. The electrical properties of the tissues in the region of interest were updated for the corresponding excitation frequency.

3. Results

We performed electromagnetic (EM) simulations of the proposed transmission line with a finite-different time difference (FDTD) software (Sim4Life by ZMT, www.zurichmedtech.com [55]). The simulations were conducted to acquire the $|B_1|$ field, the line impedance, the S parameters, and the current density.

To demonstrate the performance of the TL in the multifrequency domain, we used a current source with a central frequency at 210 MHz and a bandwidth of 400 MHz. to ensure that all the frequencies of interest would be properly analyzed. This procedure was useful for the tuning of the circuits.

All the conductors were set as perfect electric conductors, wherein the dielectric material was set as a Rogers RT/duroid 6002 with a relative permittivity of 2.94 and a

conductivity of 0.000668 S/m.

The lumped elements added for the low-frequency tuning (80, 116, and 121 MHz) consisted of two series capacitors with values equal to 75 pF and two parallel inductors with values equal to 10 nH. For the case of the high-frequency group (280 and 300 MHz), the circuit consisted of three series capacitors with values equal to 20 pF and three parallel inductors with values equal to 8 nH.

Figure 4(a) shows the impedance of the proposed line at each of the frequencies of interest. As predicted by Eq. (12), the impedance is an indicator of the upper and lower frequency boundaries and ensures operation in the frequency band and a uniform field distribution along the line. Even though the proposed line is not exactly a CRLH TL, the field response and impedance are similar to those predicted by the formulated Eq. (11). The zero crossing of the impedance phase indicates the occurrence of a resonant frequency, as show in the Fig. 4(a).

Given that the current MRI systems can only perform scans at one frequency at a time, it is needed to add individual frequency matching circuits that would need to be optimized before specific scans at selected frequencies. We used basic LC network matching circuits to achieve a 50 Ω impedance, as it is shown in Fig. 4(b) with the S_{11}
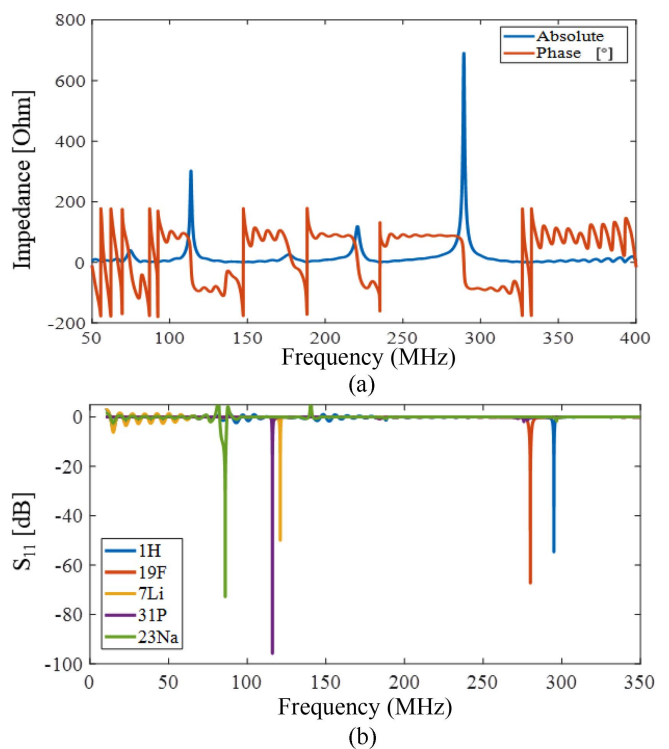

Fig. 4. (Color online) (a) Absolute and phase impedance of the transmission line, and (b) the S-parameters of the matching circuits.
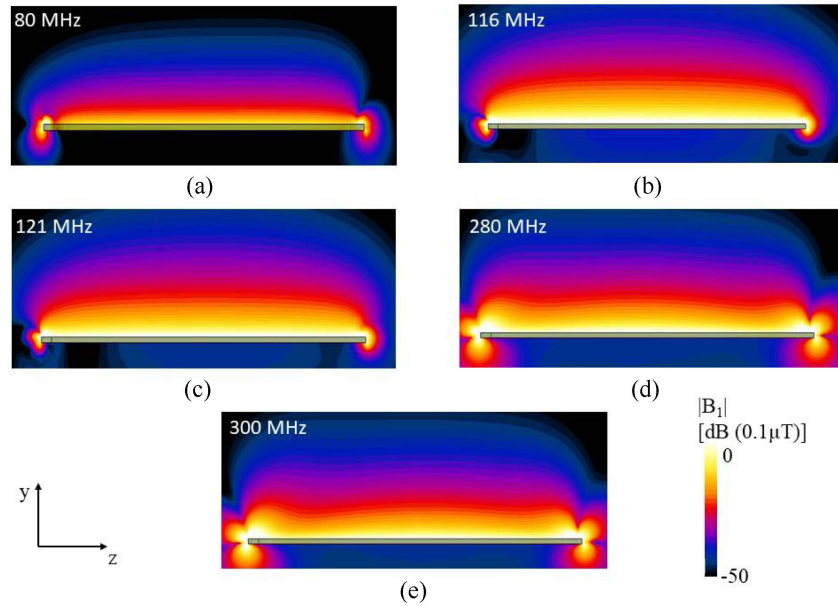
Fig. 5. (Color online) $|B_1|$ field in the Z-Y plane at (a) 80 MHz, (b) 116 MHz, (c) 121 MHz, (d) 280 MHz, and (e) 300 MHz.

parameter.

From the EM simulations we extracted the computed magnetic fields, and the $|B_1|$ field maps are shown in Fig. 5 and 6 for the Z-Y and the X-Y plane. As it can be observed, the field uniformity is similar at each frequency and along the transmission line. To check the uniformity of the field, we extracted a profile line along the X-Y

Fig. 6. (Color online) $|B_1|$ field in the X-Y plane at (a) 80 MHz, (b) 116 MHz, (c) 121 MHz, (d) 280 MHz, and (e) 300 MHz.

plane, computed the standard deviation, and normalized it with the mean value. The normalized standard deviation for the 80, 116, 121, 280 and 300 MHz were 0.15, 0.47, 6, 0.1, and 0.22, respectively. However, the standard deviation showed the relative variation of the field along the line. Accordingly, we would like to compute how centered the field was. For this reason, we also computed the skewness for which the values for the 80, 116, 121, 280, and 300 MHz were 0.27, 0.128, −0.3, 0.12, and −0.22, respectively. As it can be observed, the field is nearly uniform at each of these frequencies. A skewness value of zero represents a perfect symmetrical curve. However, it is almost impossible to obtain a value of zero. Thus, it is considered that the values between −0.5 and 0.5 are highly symmetric. The data from the profile line show that the field has skewness values within the highly symmetric range, thus indicating that the field can be considered symmetric and therefore uniform.

In addition, Fig. 7 shows the current density in the X-Z plane for each of the frequencies. Despite the amplitude differences among frequencies, it can be observed that the current has a uniform pattern along the line, and can thus produce uniform magnetic field.

To show the performance of the proposed coil in a loading condition, we also performed EM simulations to compute the $|B_1|$- field inside of the head of a human model phantom, the Fig. 8 shows the Z-Y plane B_1 field for each of the operating frequencies of the CRLH TL. The average $|B_1|$ field value was computed as 0.009, 0.006, 0.01, 0.03 and 0.04 μT for the 80, 116, 121, 280
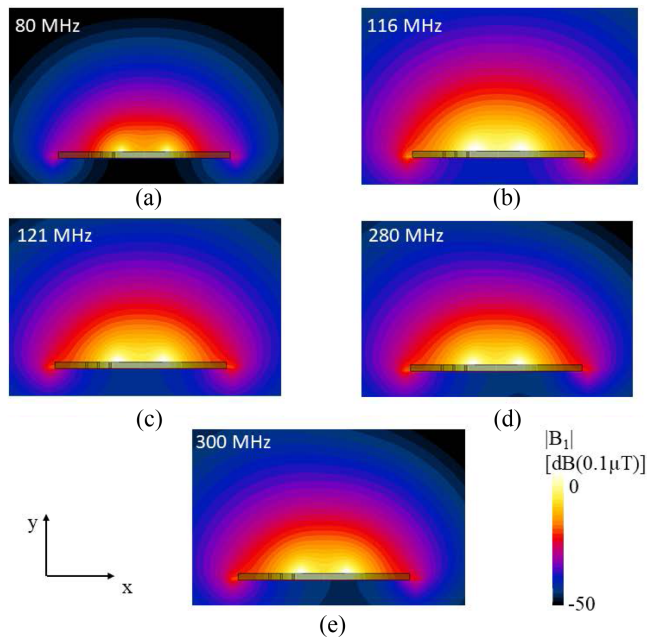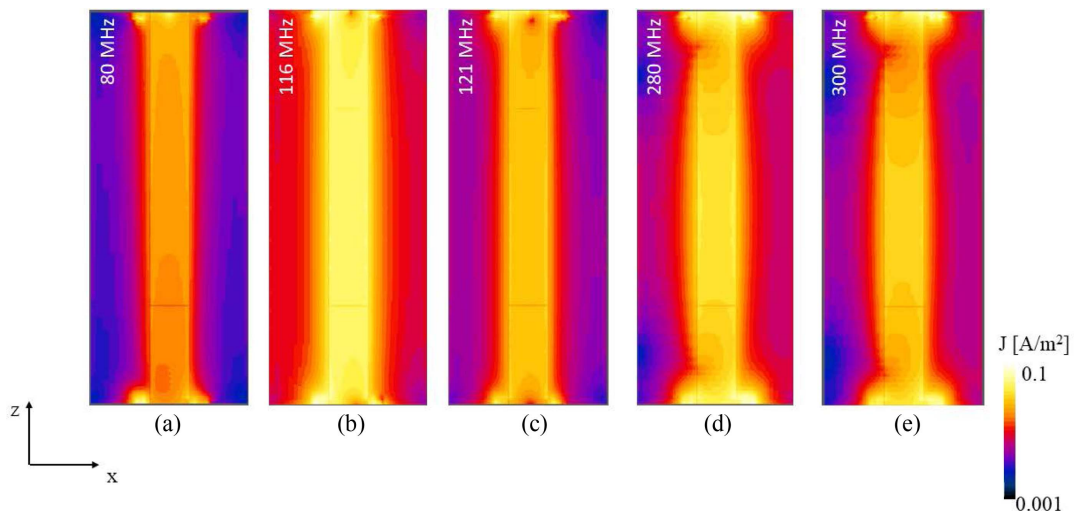
Fig. 7. (Color online) Current density J in the X-Z plane at (a) 80 MHz, (b) 116 MHz, (c) 121 MHz, (d) 280 MHz, and (e) 300 MHz.
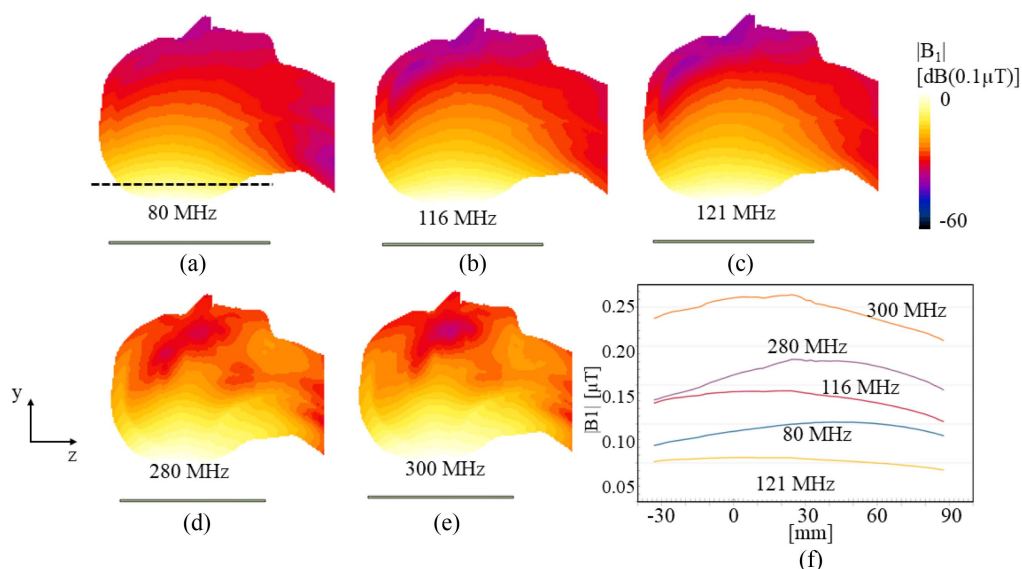

Fig. 8. (Color online) |B$_1$| field in the Z-Y plane at (a) 80 MHz, (b) 116 MHz, (c) 121 MHz, (d) 280 MHz, and (e) 300 MHz inside the human model, (f) shows the line profile of the |B$_1$| field.

and 300 MHz respectively. The difference in magnitude can be attributed to the matching quality; however the field intensity is similar for each frequency. Figure 8(f) includes a line profile plot as show by the dotted line, as it can be see the uniformity of the |B$_1$| field is similar in each frequency.

4. Conclusions

We presented the design of a transmission line that was capable of producing a uniform B$_1$ field along the Z-Y plane, wherein a modification was implemented in the microstrip according to the proposed method based on the CRLHTL concept. The proposed transmission line had a straight line without any cuts or discontinuities along the line to avoid field disturbances. The added lumped elements were placed at the end and beginning of the line. The lumped elements consisted of a series capacitance and parallel inductance that were connected to the ground through vias.

The proposed microstrip arrangement yielded a uniform field at the frequencies of interest. The impedance values were set to the frequencies that were equivalent to the X-nuclei and proton, respectively. The S$_{11}$ parameter indicated

the practical use of the proposed line. The addition of matching circuits is necessary given that currently most of the MRI scans are conducted at a single frequency. However, in future applications when multiple frequency acquisitions become possible, the proposed coil would be of tremendous interest.

Although, it is not possible to analyze the propagation constant with EM simulations, the uniformity of the B_1 field is in close agreement with theory based on the equations.

In the same manner, the current density showed that the experimentally measured current amplitudes and phases agreed with those estimated based on the equations. It should be noticed that the equations discussed in this study apply to lossless strip lines. However, the simulations were correlated with the results.

The proposed work has the potential to be used for the MRI and MRS of X-nuclei for individual frequency scanning, as well as the multifrequency scanning.

Acknowledgements

References

[1] M. A. Horsfield and D. K. Jones, NMR Biomed. **15**, 570 (2002).

[2] W. DeMartini, C. Lehman, and S. Partridge, Academic Rad. **15**, 408 (2008).

[3] W. van der Zwaag, A. Schäfer, J. P. Marques, R. Turner, and R. Trampel, NMR Biomed. **29**, 1274 (2016).

[4] O. Kraff and H. H. Quick, J. Magn. Reson. Imaging **46**, 1573 (2017).

[5] G. A. Kerchner, J. Alzheimer's Dis. **26**, 91 (2011).

[6] J. D. Poorter, Magn. Reson. Med. **34**, 359 (1995).

[7] F. Schick, H. Bongers, W. I. Jung, M. Skalej, and O. Lutz, Magn. Reson. Imag. **9**, 509 (1991).

[8] R. Hu, D. Kleimaier, M. Malzacher, M. A. Hoesl, N. K. Paschke, and L. R. Schad, J. Magn. Reson. Imaging **51**, 355 (2020).

[9] S. C. Niesporek, A. M. Nagel, and T. Platt, Top. Magn. Reson. Imaging **28**, 173 (2019).

[10] S. Konstandin and L. R. Schad, Magn. Reson. Mater. Phys. Biol. Med. **27**, 1 (2014).

[11] G. N. Holland, P. A. Bottomley, and W. S. Hinshaw, J. Magn. Reson. (1969) **28**, 133 (1977).

[12] M. Srinivas, A. Heerschap, E. T. Ahrens, C. G. Figdor, and I. J. de Vries, Trends Biotechnol. **28**, 363 (2010).

[13] J. Ruiz-Cabello, P. Walczak, D. A. Kedziorek, V. P. Chacko, A. H. Schmieder, S. A. Wickline, G. M. Lanza, and J. W. Bulte, Magn. Reson. Med. **60**, 1506 (2010).

[14] M. Srinivas, P. A. Morel, L. A. Ernst, D. H. Laidlaw, and E. T. Ahrens, Magn. Reson. Med. **58**, 725 (2007).

[15] A. N. Stevens, P. G. Morris, R. A. Iles, P. W. Sheldon, and J. R. Griffiths, Br. J. Cancer **50**, 113 (1984).

[16] J. Shani and W. Wolf, Cancer Res. **37**, 2306 (1977).

[17] A. W. Scholz, U. Wolf, M. Fabel, N. Weiler, C. P. Heussel, B. Eberle, M. David, and W. G. Schreiber, Magn. Reson. Imaging **27**, 549 (2009).

[18] J. Ruiz-Cabello, B. P. Barnett, P. A. Bottomley, and J. W. Bulte, NMR Biomed. **24**, 114 (2011).

[19] F. E. Boada, Y. Qian, A. Gildengers, M. Phillips, and D. Kupfer, ISMRM, 592 (2010).

[20] F. E. Smith, P. E. Thelwall, J. Necus, C. J. Flowers, A. M. Blamire, and D. A. Cousins, Mol. Psychiatry **23**, 2184 (2018).

[21] K. Kogure, H. Ohtomo, S. Matsui, and H. Kohno, Aims on Phosphorus-31 Magnetic Resonance Imaging. In Functional Mapping of the Brain in Vascular Disorders, Springer, Berlin, Heidelberg (1985) pp 15-28.

[22] Y. Liu, Y. Gu, and X. Yu, Quant. Imaging Med. Surg. **7**, 707 (2017).

[23] N. J. Shah, W. A. Worthoff, and K. J. Langen, NMR Biomed. **29**, 162 (2016).

[24] K. Huhn, T. Engelhorn, R. A. Linker, and A. M. Nagel, Frontiers Neurol. **10**, 84 (2019).

[25] M. Inglese, G. Madelin, N. Oesingmann, J. S. Babb, W. Wu, B. Stoeckel, J. Herbert, and G. Johnson, Brain **133**, 847 (2010).

[26] K. L. Zakian, J. A. Koutcher, and D. Ballon, Magn. Res. Med. **41**, 809 (1999).

[27] A. Yahya, N. De Zanche, and P. S. Allen, NMR BIOMED **26**, 533 (2013).

[28] S. M. Hong, C. H. Choi, A. W. Magill, N. J. Shah, and J. Felder, IEEE Trans. Med. Imaging **37**, 2613 (2018).

[29] S. Goluch, A. Kuehne, M. Meyerspeer, R. Kriegl, A. I. Schmid, G. B. Fiedler, and J. Bernarding, Magn. Reson. Med. **73**, 2376 (2015).

[30] E. A. Mellon, D. T. Pilkinton, C. M. Clark, M. A. Elliott, W. R. Witschey, A. Borthakur, and R. Reddy, Am. J. Neuroradiol. **30**, 978 (2009).

[31] C. H. Choi, S. M. Hong, J. Felder, and N. J. Shah, Magn. Reson. **279**, 11 (2017).

[32] F. Du, S. Liu, Q. Chen, N. Li, Y. Dou, X. Yang, Z. Wang, X. Zhang, B. Shen, and Y. Li, IEEE Trans. Magn. **54**, 1 (2018).

[33] C. Wang, Y. Li, B. Wu, D. Xu, S. J. Nelson, D. B. Vigneron, and X. Zhang, Magn. Reson. Imaging **30**, 78 (2012).

[34] Y. Pang, Z. Xie, D. Xu, D. A. Kelley, S. J. Nelson, D. B. Vigneron, and X. Zhang, Magn. Reson. Imaging **30**, 290 (2012).

[35] Y. Duan, B. S. Peterson, F. Liu, T. R. Brown, T. S. Ibra-

him, and A. J. Kangarlu, Magn. Reson. Imaging **29**, 13 (2009).

[36] G. Lykowsky, F. Carinci, M. Düring, D. Weber, P. M. Jakob, and D. Haddad, Quant. Imaging Med. Surg. **5**, 799 (2015).

[37] G. C. Wiggins, R. Brown, and K. Lakshmanan, NMR Biomed. **29**, 96 (2016).

[38] K. N. Kim, D. Hernandez, J. H. Seo, Y. Noh, Y. Han, Y. C. Ryu, and J. Y. Chung, Plos One **14**, e0219407 (2019).

[39] A. Kumar, W. A. Edelstein, and P. A. Bottomley, Magn. Reson. Med. **61**, 1201 (2009).

[40] O. Marrufo and A. O. Rodriguez, In 2005 IEEE Eng. Med. Biol. 27th Ann. Conf. 2006 Jan 17 (pp 4282-4285).

[41] P. A. Bottomley, C. H. Olivieri, and R. Giaquinto, Magn. Reson. Med. **37**, 591 (1997).

[42] D. J. Larkman, The G-factor and Coil Design. In Parallel Imaging in Clinical MR Applications, Springer, Berlin, Heidelberg (2007) pp 37-48.

[43] S. J. Salama, King Saud Univ. -Eng. Sci. **32**, 42 (2020).

[44] C. Constantinides and S. Angeli, J. Magn. Res. **222**, 59 (2012).

[45] S. D. Han, P. Heo, H. J. Kim, H. Song, D. Kim, J. H. Seo, Y. Ryu, Y. Noh, and K. N. Kim, Concepts Magn. Reson. Part B: Magn. Reson. Eng. **47**, e21363 (2017).

[46] X. Yan, J. C. Gore, and W. A. Grissom, Nat. Commun. **9**, 1 (2018).

[47] G. C. Wiggins, J. R. Polimeni, A. Potthast, M. Schmitt, V. Alagappan, and L. L. Wald, Magn. Reson. Med. **62**, 754 (2009).

[48] P. B. Roemer, W. A. Edelstein, C. E. Hayes, S. P. Souza, and O. M. Mueller, Magn. Reson. Med. **16**, 192 (1990).

[49] X. Zhang, K. Ugurbil, and W. Chen, Magn. Reson. Med. **46**, 443 (2001).

[50] R. F. Lee, C. R. Westgate, R. G. Weiss, D. C. Newman, and P. A. Bottomley, Magn. Reson. Med. **45**, 673 (2001).

[51] A. Lai, T. Itoh, and C. Caloz, IEEE Microw. Mag. **5**, 34 (2004).

[52] A. Hurshkainen, A. Nikulin, E. Georget, B. Larrat, D. Berrahou, A. L. Neves, P. Sabouroux, S. Enoch, I. Melchakova, P. Belov, and S. Glybovski, Sci. Rep. **8**, 1 (2018).

[53] A. Rennings, J. Mosig, A. Bahr, C. Caloz, M. E. Ladd, and D. Erni, In 2009 3rd Eur. Conf. Antennas Propag. 2009 Mar 23 (pp 3231-3234).

[54] A. Christ, Phys. Med. Biol. **55**, (2009).

[55] Sim4Life by ZMT, www.zurichmedtech.com